RSC Advances

PAPER

View Article Online
View Journal | View Issue

Cite this: *RSC Adv.*, 2025, **15**, 2205

Optimizing adsorption and photocatalysis for tetracycline and sulfamethoxazole removal: the role of Ag^+ and NH_4^+ in Bi-MOF derivatives

Vy Anh Tran, *[a] Thi Tuong Vi Tran,[a] Tran Thanh Sang,[b] Nguyen Anh Thu,[b] Nguyen Duy Dat,[b] Hieu Vu_Quang,[c] Van Thuan Le*[d] and Thu Thao Thi Vo*[e]

This study focuses on the synthesis, characterization, and evaluation of the photocatalytic efficiency of bismuth-based metal–organic frameworks (Bi-MOFs) and their derivatives, specifically Ag^+/Bi-MOF and NH_4^+/Ag^+/Bi-MOF, in the degradation of tetracycline (TC) and sulfamethoxazole (SMX) under visible light irradiation. Bi-MOFs are promising photocatalysts due to their large surface area, tunable porosity, and unique electronic properties that are favorable for visible light absorption. In this study, Bi-MOFs were synthesized using a solvothermal method, with the incorporation of silver (Ag^+) and ammonium (NH_4^+) ions to enhance their photocatalytic performance. The photocatalytic activity of Bi-MOF, Ag/Bi-MOF, and NH_4^+/Ag^+/Bi-MOF was evaluated by measuring the degradation rates of TC and SMX in aqueous solutions under visible light. The experiments demonstrated that Bi-MOFs effectively degraded both antibiotics, with the Ag/Bi-MOF derivative showing superior performance due to improved charge separation and light absorption. NH_4^+/Ag^+/Bi-MOF also exhibited significant photocatalytic activity, influenced by the presence of ammonium ions, which altered the surface chemistry of the catalyst and affected the adsorption and degradation processes. Reusability tests confirmed that these photocatalysts maintained high degradation efficiency over multiple cycles, highlighting their potential for practical environmental applications. This research provides a sustainable and effective solution for the removal of persistent organic pollutants such as TC and SMX.

Received 11th October 2024
Accepted 13th January 2025

DOI: 10.1039/d4ra07287a

rsc.li/rsc-advances

1. Introduction

The increasing contamination of water sources by organic pollutants, especially pharmaceutical compounds such as antibiotics, has become a critical environmental issue worldwide.[1,2] Among these contaminants, tetracycline (TC) and sulfamethoxazole (SMX) are two widely used antibiotics that are frequently detected in various water bodies.[3] These antibiotics enter the environment through multiple pathways, including pharmaceutical industry discharge, agricultural runoff, and improper disposal of unused medications.[4] The presence of such pollutants in water sources poses a serious threat to aquatic ecosystems and human health, as they can contribute to the development of antibiotic-resistant bacteria, disrupt aquatic life, and even enter the human food chain.[5]

Traditional water treatment methods, including biological processes, chemical oxidation, and filtration, have proven inadequate in completely removing these persistent organic pollutants (POPs) from contaminated water.[6,7] This inadequacy has spurred the search for alternative and more effective treatment technologies. In recent years, photocatalysis has emerged as a promising approach for the degradation of POPs in water, utilizing light energy to activate catalysts that can break down organic molecules into less harmful substances.[8,9] However, the efficiency of photocatalysis largely depends on the type of catalyst used, its stability, and its ability to absorb light in the visible spectrum.

Metal–organic frameworks (MOFs) have attracted significant attention in the field of photocatalysis due to their unique properties, such as high surface area,[10] tunable porosity,[11] and the ability to incorporate various metal ions.[12–14] MOFs are crystalline materials composed of metal ions or clusters coordinated to organic ligands, forming a porous network.[15,16] The versatility in the design and synthesis of MOFs allows for the creation of materials with specific properties tailored to

[a]*Department of Material Science, Institute of Applied Technology and Sustainable Development, Nguyen Tat Thanh University, Ho Chi Minh City, 700000, Vietnam. E-mail: tavy@ntt.edu.vn*

[b]*Faculty of Chemical & Food Technology, University of Technology and Education, Thu Duc, Ho Chi Minh City 700000, Vietnam*

[c]*NTT Hi-tech Institute, Nguyen Tat Thanh University, Ho Chi Minh City, 700000, Vietnam*

[d]*Center for Advanced Chemistry, Institute of Research and Development, Duy Tan University, 03 Quang Trung, Da Nang, 550000, Vietnam. E-mail: levanthuan3@duytan.edu.vn*

[e]*Department of Food Science and Biotechnology, Gachon University, 1342 Seongnamdaero, Sujeong-gu, Seongnam-si, 13120, Republic of Korea. E-mail: vothuthaobd@gmail.com*

particular applications.[17,18] Among the various types of MOFs, bismuth-based MOFs (Bi-MOFs) have shown great potential in photocatalytic applications, particularly for environmental remediation.[19,20]

Bismuth (Bi) is a heavy metal with unique electronic properties, including a large atomic radius, a high charge-to-size ratio, and the ability to form strong bonds with oxygen and nitrogen-containing ligands.[21,22] These properties make bismuth an ideal candidate for photocatalysis, as it can effectively absorb visible light and participate in redox reactions.[23,24] The incorporation of bismuth into MOFs results in materials with enhanced photocatalytic properties, capable of degrading organic pollutants under visible light irradiation.[25–27] Moreover, the high stability and reusability of Bi-MOFs make them attractive for practical applications in water treatment.[28,29]

In this study, we focus on the synthesis, characterization, and photocatalytic evaluation of Bi-MOFs and their derivatives, specifically Ag/Bi-MOF and NH_4^+/Ag^+/Bi-MOF. The rationale behind incorporating silver (Ag^+) and ammonium (NH_4^+) into the Bi-MOF structure lies in their potential to further enhance the photocatalytic performance of the material. Silver ions are known for their antimicrobial properties and ability to improve the charge separation efficiency in photocatalysts, which can lead to higher photocatalytic activity. On the other hand, ammonium ions can influence the acidity of the environment and alter the surface chemistry of the photocatalyst, potentially affecting the adsorption and degradation processes of the target pollutants.

2. Methods & experiment

2.1. Chemical materials

Sigma-Aldrich provided the following materials: 1,4-benzoic acid, bismuth(III) nitrate pentahydrate, silver nitrate, sulfamethoxazole, tetracycline, ammonium chloride, *N*,*N*-dimethylformamide, sulfuric acid (0.1 N), and sodium hydroxide. Both HPLC-grade water and ethanol were used just as they were, without any further purification. The remaining reagents were all of the best quality that was commercially available, and they were all used exactly as given. After thoroughly cleaning the glassware with a 3 : 1 HNO_3 solution, it was rinsed several times with deionized (DI) water.

2.2. Synthesis of pristine bismuth-MOF nanomaterial (Bi-MOF)

12 mmol of $Bi(NO_3)_3 \cdot 5H_2O$ (5.82 g) and 18 mmol of H_2BDC (2.99 g) are dissolved in 100 mL of DMF to create a solution. After that, this mixture is agitated for 20 minutes at 600 rpm until it dissolves and turns clear. The resultant mixture is then put into an autoclave lined with Teflon and heated to 120 °C for 60 hours. The mixture is centrifuged three times at 600 rpm for fifteen minutes after it has cooled to room temperature. The catalyst is then separated after the mixture is cleaned with DMF. To make sure all leftover materials are gone, it goes through three further rounds of centrifugation at 600 rpm for ten minutes while using 100 mL of ethanol. To produce Bi-MOF, the mixture is lastly dried for 24 hours at 120 °C.

2.3. Synthesis of Ag^+/Bi-MOF and NH_4^+/Ag^+/Bi-MOF nanomaterial

For the $AgNO_3$: $Bi(NO_3)_3 \cdot 5H_2O$ molar ratio, weigh 1.02 grams of $AgNO_3$ (6 mmol) and 5.82 grams of $Bi(NO_3)_3 \cdot 5H_2O$ (12 mmol). Add them to 100 milliliters of DMF and stir until the mixture becomes clear about 30 minutes. Place the transparent solution into an autoclave coated with Teflon and close it firmly. After 60 hours of heating the autoclave to 120 °C, let the mixture cool to ambient temperature. Centrifuge the mixture three times at 3000 rpm for ten minutes to get rid of any leftover reactants. Repeat steps three times: wash mixture with DMF, separate catalyst, and centrifuge again at 300 rpm for 20 minutes using around 100 mL of ethanol. To create the Ag^+/Bi-MOF product, dry the final combination that was obtained following the washing operation for a full day at 120 °C.

2.4. Adsorption experiments

At 25 °C, batch tests were conducted to evaluate the adsorption efficiency of Ag^+/Bi-MOF, NH_4^+/Ag^+/Bi-MOF, and Bi-MOF. In the trials, predetermined concentrations of TC and SMX were dissolved in deionized (DI) water. 50 mg of Bi-MOF, Ag^+/Bi-MOF, or NH_4^+ Ag^+/Bi-MOF were suspended in 100 mL of a pH 7 solution containing 20 ppm TC or SMX during the first cycle of the adsorption procedure. After one minute of sonication, the mixture was moved to a reactor and agitated for thirty minutes at 25 °C at 400 rpm using a magnetic stirrer. Water flowing in an outer jacket around the reactor maintained its temperature constant. Centrifugation was used to separate the adsorbent from the solution. To eliminate TC or SMX from the Bi-MOF, Ag^+/Bi-MOF, or NH_4^+/Ag^+/Bi-MOF, the adsorbent was continuously stirred while being submerged in a large amount of ethanol solvent. The Bi-MOF variants were then dried in a vacuum oven in preparation for more testing.

2.5 Photocatalytic experiments

By calculating the photodegradation percentage of TC/SMX in an aqueous solution exposed to visible light, the sample's photocatalytic performance was evaluated. The simulation visible light source was a 250 W high-pressure mercury lamp (Mercury HPL-N 250W). The light source was filtered to primarily emit wavelengths between 400 nm and 700 nm, aligning with the visible spectrum. Generally, 100 mL of TC/SMX solution was placed in a photoreactor together with 50 mg of each kind of nanomaterial photocatalyst. By moving cooling water through an outer jacket around the reactor, the temperature of the photoreactor was kept constant at 25 °C. To attain adsorption–desorption equilibrium, the solution was agitated for 30 minutes in the dark before light exposure. Next, simulation visible light was introduced to the solution. To separate the photocatalysts, 3 mL aliquots were removed from the photoreactor and centrifuged at predetermined intervals. The proportion of TC/SMX photodegradation was tracked using the supernatant. The TC/SMX sample's absorbance was

measured, and the solution's absorption wavelengths were noted.

The degradation efficiency (DE, %) was calculated based on the initial and final concentrations of the target pollutants, using the formula:

$$\text{Degradation efficiency}(\%) = \frac{C_0 - C_t}{C_0} \times 100 \quad (1)$$

where C_0 is the initial concentration of the TC/SMX pollutant, and C_t is its concentration at time t.

The reduction in Chemical Oxygen Demand (COD) and Total Organic Carbon (TOC) was evaluated to determine the degree of mineralization. TOC values were measured using a Multi N/S 2100S TOC analyzer (Analytik Jena, Germany). COD measurements were conducted using the dichromate oxidation method with a COD reactor HI839150 (Hanna Instruments, Vietnam). The percentage COD and TOC reductions were calculated by eqn (2) and (3), respectively.

$$\%\text{COD reduction} = \frac{\text{COD}_{\text{initial}} - \text{COD}_{\text{final}}}{\text{COD}_{\text{initial}}} \times 100 \quad (2)$$

$$\%\text{TOC reduction} = \frac{\text{TOC}_{\text{initial}} - \text{TOC}_{\text{final}}}{\text{TOC}_{\text{initial}}} \times 100 \quad (3)$$

Here, $\text{COD}_{\text{initial}}$ and $\text{TOC}_{\text{initial}}$ are the initial COD and TOC values, while $\text{COD}_{\text{final}}$ and $\text{TOC}_{\text{final}}$ represent the final values after reaction.

2.6. Physicochemical properties of MOF nanomaterials

2.6.1 Fourier transform infrared spectra (FTIR). A little portion of the powder sample, free of any hygroscopic substance, is sandwiched between two support plates after it has been freeze-dried. A Vertex 70 FTIR spectrometer (Bruker, USA) was used to record the FTIR spectra.

2.6.2 Scanning electron microscopy (SEM). The surface morphology of the MOF samples was investigated using a Hitachi S-4700 FE-SEM (Japan) operating at a 15 kV accelerating voltage. After the samples dried, they were applied to cover glasses measuring 22 by 22 mm, which were subsequently fastened to polished aluminum stubs with carbon tape. To improve the precision of size measurements in SEM analysis, no palladium nor gold coating was applied to the samples. All sample solutions were treated in an ultrasonic bath for 30 seconds and then blended with a vortex mixer for 20 seconds before being applied to the glass to reduce nanoparticle agglomeration.

2.6.3 Nitrogen physisorption isotherms. Nitrogen physisorption isotherm analysis was performed using the Nova Station C instrument from Quantachrome Instruments, utilizing the NovaWin version 11.0 software for data acquisition and processing. Using volumetric equipment, nitrogen physisorption isotherms were recorded at −196 °C. Samples were outgassed in a vacuum at room temperature for at least thirty hours before testing. The Brunauer–Emmett–Teller (BET) method was utilized to compute surface areas, and the Barrett–Joyner–Halenda (BJH) approach was applied to ascertain the mesopore size distribution.

2.6.4 X-ray diffraction. An X-ray automated diffractometer (Rigaku Rint 2200 Series, Rigaku, Japan) working in continuous-scanning 2θ mode (40 kV, 30 mA) was used to create the XRD patterns of the nanoparticles. Monochromatized Cu Kα1 radiation at 1.5406 Å wavelength was used to form the patterns.

3. Results & discussion

3.1. Preparation and characterization of as-prepared samples

3.1.1 Synthesis process. The process begins with dissolving bismuth precursors (Bi^{3+}) and organic ligands (typically carboxylic acid or its derivatives) in a suitable solvent such as DMF (dimethylformamide). The mixture is then heated under high temperature in a sealed system (solvothermal process). During this process, Bi^{3+} ions interact with the carboxylate groups of the ligand, forming coordination bonds to create the 3D network structure of Bi-MOF. Subsequently, Ag^+ ions can diffuse into the pores or surface of the Bi-MOF and interact with functional groups within the MOF, such as carboxylate or hydroxyl groups. Ag^+ may create silver nanoparticles on the surface or within the porous structure of Bi-MOF through aggregation or the formation of complex bonds between Ag^+ and organic ligands. In the next step, NH_4^+ can interact with other functional groups in Bi-MOF, such as N–H or amino groups, in addition to the interaction with Ag^+. The presence of NH_4^+ can affect the pH of the solution and cause changes in the surface chemical structure of Bi-MOF. NH_4^+ and Ag^+ ions interact with the ligands, forming complex bonds or enhancing existing bonds.

The formation process of the materials in Fig. 1a reflects the complexity and flexibility in designing photocatalytic materials. Each additional step (Ag^+ and NH_4^+) not only alters the physical structure of the material but also enhances its chemical and catalytic properties. Ag^+ plays a crucial role in improving charge separation, while NH_4^+ can influence adsorption and degradation processes. The final result is the creation of materials with high photocatalytic efficiency, suitable for applications in environmental treatment.

3.1.2 TGA analysis. TGA measures the change in the mass of a material as the temperature increases. This helps identify thermal decomposition processes, water loss, or the evaporation of compounds within the material. In the first stage, TGA shows a small weight loss below 100 °C, which may be related to the physical loss of water or the evaporation of solvents retained in the material. In the next stage, significant weight loss at higher temperatures (from 500 °C to 600 °C) is due to the decomposition of organic ligands in Bi-MOF or the breakdown of the MOF framework.[30,31] In the final stage, the material's mass does not change significantly, indicating that the remaining material (typically metal oxides or non-volatile solids) possesses high thermal stability (Fig. 1b).

3.1.3 BET analysis. Fig. 1c provides information related to material properties such as surface area, pore volume, and pore size of the Bi-MOF and NH_4^+/Ag^+/Bi-MOF samples. Bi-MOF may have a large surface area, which contributes to its adsorption and catalytic capabilities. A large surface area allows more

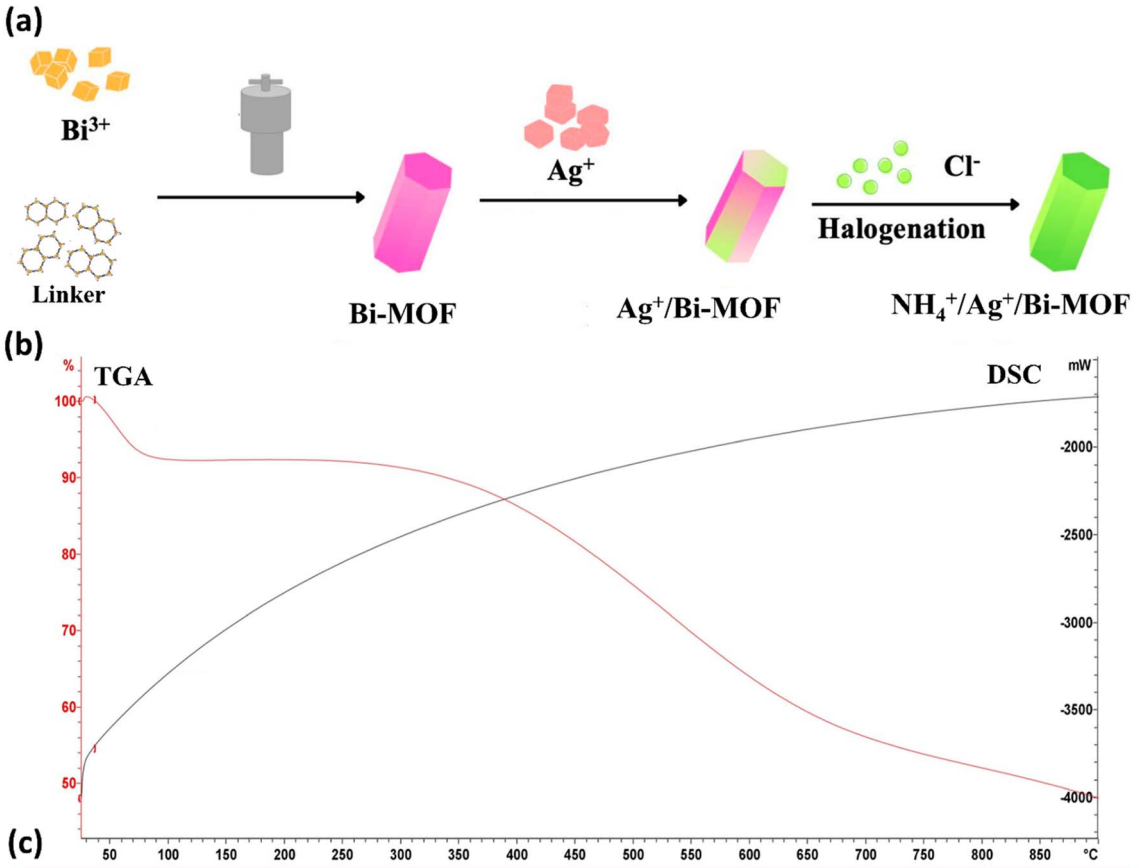

Nanomaterial	S_{BET} (m^2/g)	V_{pore} (cm^3/g)	d_{pore} (nm)
Bi-MOF	38.1	0.122	2.8
NH_4^+/Ag^+/Bi-MOF	21.2	0.084	2.4

Fig. 1 (a) Illustrative diagram of the synthesis process of Bi-MOF, Ag^+/Bi-MOF, and NH_4^+/Ag^+/Bi-MOF; (b) thermogravimetric analysis (TGA) and differential scanning calorimetry (DSC) of Bi-MOF; (c) BET results of Bi-MOF and NH_4^+/Ag^+/Bi-MOF.

pollutant molecules to come into contact with the catalytic surface, enhancing degradation efficiency. In the case of NH_4^+/Ag^+/Bi-MOF, the surface area decreases, possibly due to the presence of NH_4^+/Ag^+ within the pores of Bi-MOF or surface modifications caused by the presence of NH_4^+ and Ag^+ ions.

The large pore volume of Bi-MOF can provide more space for the adsorption of antibiotic molecules of suitable size, thereby improving catalytic efficiency. Conversely, NH_4^+/Ag^+/Bi-MOF has a smaller pore volume compared to Bi-MOF. Additionally, pore size affects the diffusion of molecules into and out of the material. In the case of NH_4^+/Ag^+/Bi-MOF, it has smaller pore sizes, this increases the selectivity for antibiotics with smaller molecular sizes like tetracycline or larger molecules like sulfamethoxazole.[32,33]

3.1.4 XRD analysis. The X-ray diffraction (XRD) patterns of Bi-MOF and its derivatives exhibit characteristic diffraction peaks, representing specific crystallographic planes within the material's structure (Fig. 2a). The XRD pattern of Bi-MOF shows sharp diffraction peaks, indicating that the material possesses a high degree of crystallinity. The peak at $2\theta \approx 24.3°$ corresponds to the (003) plane, which is a characteristic reflection of Bi-MOF. Additional peaks at $2\theta \approx 27.4°$, 30.1°, 33.5°, 42.4°, 46.3°, and 52.6° represent the (101), (110), (102), (112), (200), and (113) planes, respectively. These peaks correspond to specific planes in the crystal lattice of Bi-MOF, demonstrating that the synthesis process successfully produced a stable and uniform crystalline structure. The changes in intensity observed in the XRD pattern of Ag^+/Bi-MOF suggest that Ag^+ has been incorporated into the Bi-MOF structure, potentially creating electron traps within the crystal lattice, which could enhance photocatalytic efficiency. The alterations in the XRD pattern of NH_4^+/Ag^+/Bi-MOF indicate that the combination of NH_4^+ and Ag^+ has significantly impacted the crystalline structure. This may lead to changes in the surface properties of the material.[34,35]

3.1.5 FTIR analysis. The FTIR spectrum of Bi-MOF nanorods reveals several key features indicative of the material's structure and composition (Fig. 2b). The peak in the 1681 cm^{-1}

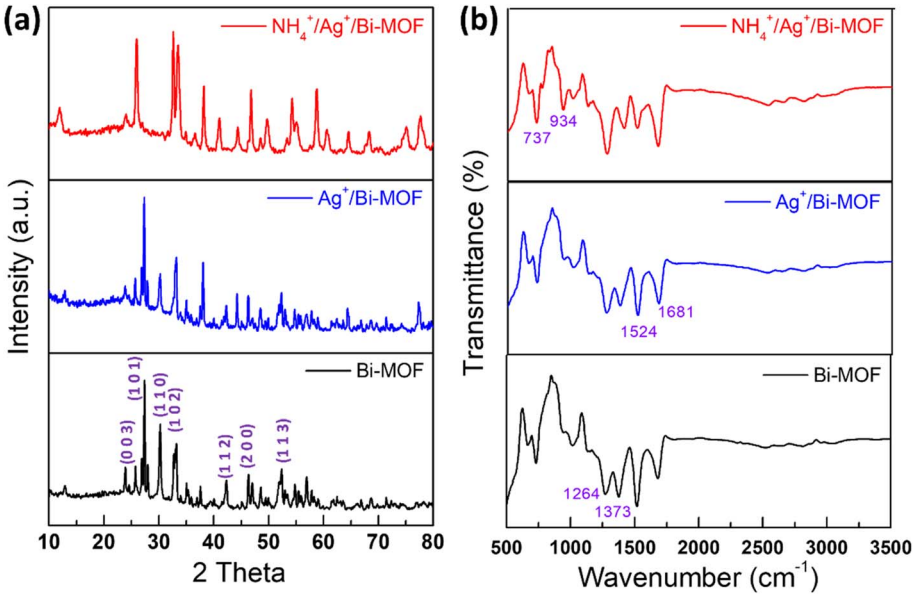

Fig. 2 (a) XRD spectra of Bi-MOF, Ag^+/Bi-MOF, NH_4^+/Ag^+/Bi-MOF, (b) FTIR spectra of Bi-MOF, Ag^+/Bi-MOF, NH_4^+/Ag^+/Bi-MOF.

range indicates the presence of carbonyl groups (C=O), common in carboxylate ligands used in Bi-MOF. Peaks in the 1524 cm^{-1} range are associated with the C=C stretching vibrations of aromatic rings. The 1373 cm^{-1} range features peaks due to the stretching vibrations of C–O bonds in carboxylate groups and Bi–O bonds, indicating the coordination of bismuth ions with oxygen atoms from the ligands. The region of 737 cm^{-1}, and 500 cm^{-1}, contains a series of peaks corresponding to bending and stretching vibrations of various bonds unique to the specific Bi-MOF structure.[36,37]

When Ag^+ is added to Bi-MOF, the FTIR spectrum of Ag^+/Bi-MOF may show slight changes in the intensity and position of certain absorption bands. The absorption bands similar to those of Bi-MOF still appear, indicating that the overall MOF structure does not significantly change after the addition of Ag^+. However, there is a shift or change in the intensity of absorption bands related to the C=O or C–O groups, suggesting the interaction of Ag^+ with the ligands in the MOF. This change may be due to the formation of complex bonds between Ag^+ and the functional groups within the MOF structure, which could enhance the photocatalytic efficiency of the material.

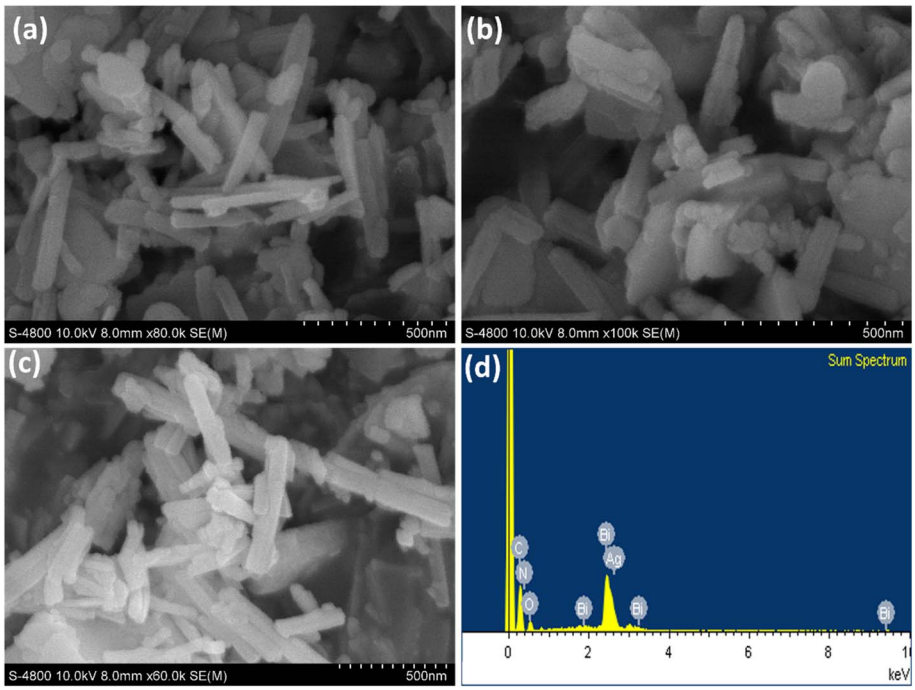

Fig. 3 SEM images of (a) Bi-MOF, (b) Ag^+/Bi-MOF, (c) NH_4^+/Ag^+/Bi-MOF, and (d) EDX spectrum of NH_4^+/Ag^+/Bi-MOF.

The FTIR spectrum of NH_4^+/Ag^+/Bi-MOF may display similar characteristics to Ag^+/Bi-MOF but with some additional changes. Absorption bands related to the N–H group may appear around 3600 cm^{-1}, representing the presence of ammonium ions (NH_4^+). Changes in the intensity or position of absorption bands in the region of 1000–1650 cm^{-1} may indicate the interaction of both NH_4^+ and Ag^+ with the functional groups in the MOF, leading to alterations in the surface chemical structure of the material. These changes could result in improved adsorption capacity and enhanced pollutant degradation efficiency, due to the formation of new bonds or the strengthening of existing bonds between the MOF components and the added ions.

3.1.6 SEM analysis. The SEM image of Bi-MOF reveals the morphological structure of the material, characterized by the presence of uniformly sized nanorods distributed evenly. The surface of Bi-MOF exhibits porosity and a large surface area, which are crucial for its photocatalytic efficiency. The crystalline nature of the Bi-MOF indicates that the synthesis process has produced a material with high crystallinity and a stable structure (Fig. 3a). Using image analysis software (ImageJ), the Bi-MOF nanorods were found to have lengths ranging from approximately 340 nm to 610 nm. Additionally, the average diameter of the nanorods was determined to be between 50 nm and 72 nm.

When Ag^+ ions are introduced into the Bi-MOF structure, the SEM image shows no change in the nanorod morphology (Fig. 3b). The crystals retain the original morphology of Bi-MOF; however, the appearance of smaller particles on the surface may be due to Ag^+ ions creating dispersed metal nanoparticles on the Bi-MOF surface. These particles could play an important role in enhancing photocatalytic efficiency by providing electron traps, which help reduce the recombination rate of electron–hole pairs.

The SEM image of NH_4^+/Ag^+/Bi-MOF shows a more complex structure with the presence of smaller particles and a rougher surface compared to the previous two samples. This could be due to the combination of NH_4^+ and Ag^+ ions causing changes in the surface structure. The small particles uniformly distributed on the surface may result from the aggregation of metal ions, contributing to changes in the surface chemistry of the catalyst, which in turn affects the adsorption and degradation processes of pollutants (Fig. 3c). The EDX spectrum shows the presence of elements including silver, bismuth, carbon, nitrogen, and oxygen, reflecting the chemical composition of NH_4^+/Ag^+/Bi-MOF. The peaks below 1 keV indicate the presence of organic elements from the ligands in the MOF structure. The

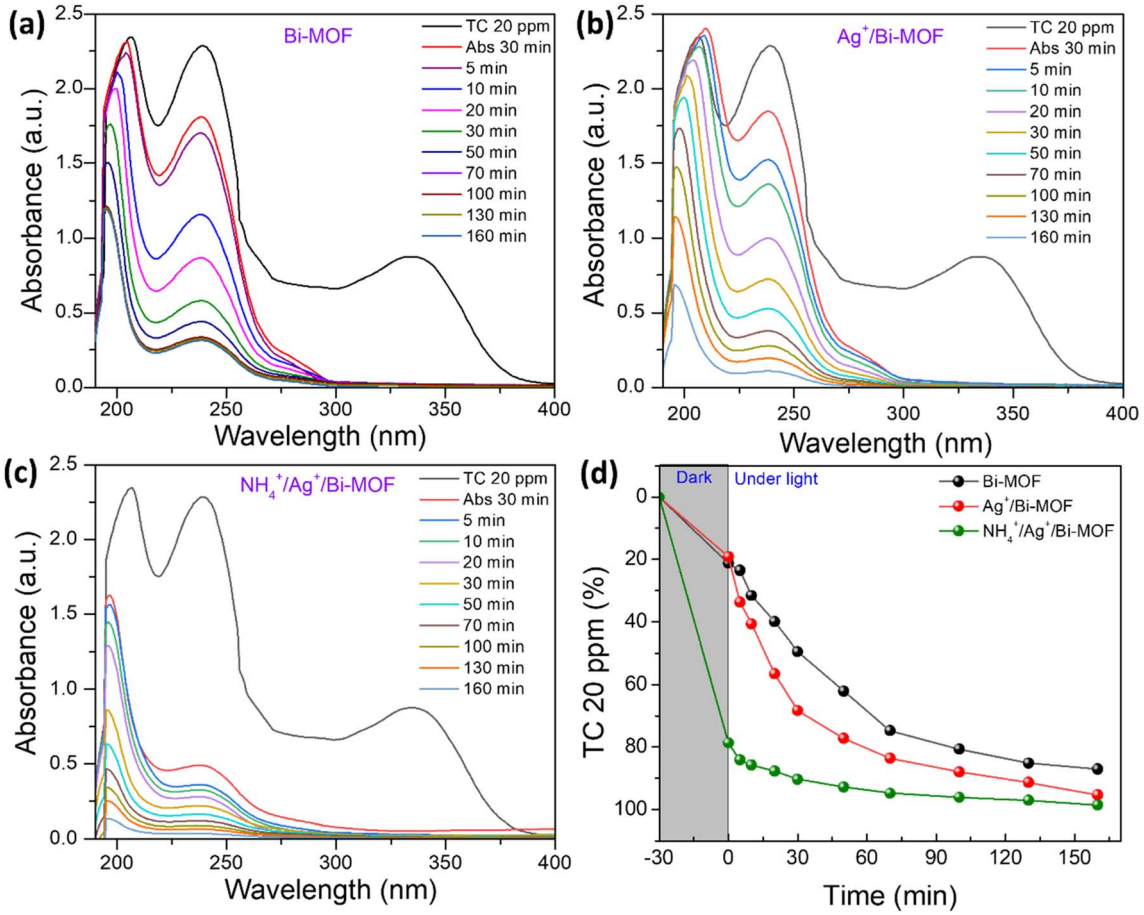

Fig. 4 UV-Vis absorption and photocatalysis of (a) Bi-MOF (pH 6.2), (b) Ag^+/Bi-MOF (pH 6.2), and (c) NH_4^+/Ag^+/Bi-MOF (pH 5.8) for the removal of TC at 27 °C; (d) summary of degradation of TC under visible light by Bi-MOF, Ag^+/Bi-MOF, NH_4^+/Ag^+/Bi-MOF.

prominent peak for Ag at 2.6 keV demonstrates that Ag^+ ions have been successfully incorporated into the MOF structure. The Bi peaks at 1.9, 2.5, 3.3, and 9.4 keV confirm the strong presence of Bismuth as part of the MOF framework (Fig. 3d).

3.2. Adsorption and photocatalytic activity investigation

3.2.1 Affinity of tetracycline complex formation with Bi-MOF compared to Ag^+ and NH_4^+. Tetracycline can form complexes with various metal ions, including Bi^{3+}, Ag^+, and NH_4^+. The preference for complex formation with one ion over another depends on several factors, such as TC's affinity for each metal ion, the chemical properties of the ions, ion concentration, and the presence of other ligands.[38,39] The complex formation process is demonstrated by the shift in peaks from three peaks at 335 nm, 238 nm, and 206 nm to 238 nm and 208 nm, as shown in Fig. 4a. In this case, tetracycline preferentially forms a complex with Bi^{3+} in the Bi-MOF structure. Despite the presence of Ag^+ and NH_4^+, tetracycline still forms a stable complex with Bi-MOF. This is evidenced by the consistent peak shift in the UV-Vis spectra shown in Fig. 4a–c.

Bi^{3+} has a high affinity for the oxygen and nitrogen atoms in TC's structure, particularly with functional groups such as –OH and $–NH_2$. TC can form strong complexes with Bi^{3+} through bonding with these functional groups. Additionally, Bi^{3+}, as a heavy metal ion, can form very stable complexes due to its high charge (3^+), making the bond between Bi^{3+} and TC stronger than those with ions of lower charge. Moreover, the porous structure of Bi-MOF is suitably sized to allow the diffusion of small molecules like tetracycline, which facilitates the complex formation between tetracycline and Bi^{3+}.

In contrast, Ag^+ has a good affinity for sulfur and nitrogen atoms. However, since TC does not contain sulfur groups, its interaction with Ag^+ mainly occurs through the –OH and $–NH_2$ groups, similar to Bi^{3+}. Although Ag^+ can form complexes with TC, these complexes are generally less stable than those with Bi^{3+} because Ag^+ only has a 1^+ charge, leading to a weaker attraction between the ion and the functional groups.

3.2.2 Influence of Bi-MOF structure and the presence of Ag^+. Sulfamethoxazole does not form a complex with bismuth-MOF because the Bi^{3+} ions are fixed within the MOF structure and cannot interact directly with SMX. However, when free Ag^+ ions are present in the solution, SMX can easily form a complex with Ag^+ due to Ag^+'s flexibility and ability to directly interact with the functional groups in SMX.[40,41]

Bi-MOF is a complex structure where bismuth ions (Bi^{3+}) are incorporated into a network with organic ligands. In this structure, the Bi^{3+} ions are not free but are tightly coordinated

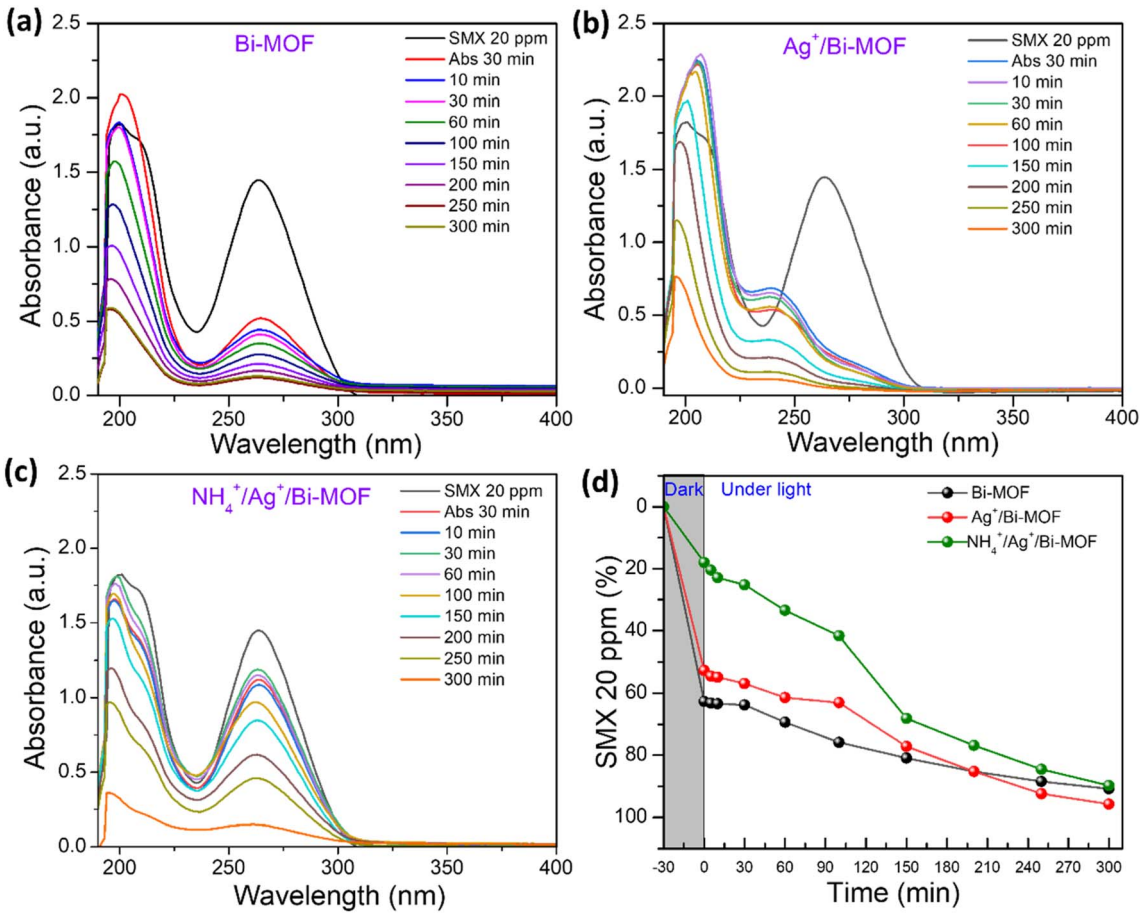

Fig. 5 UV-Vis absorption and photocatalysis of (a) Bi-MOF (pH 6.4), (b) Ag^+/Bi-MOF (pH 6.4), and (c) NH_4^+/Ag^+/Bi-MOF (pH 6.0) for the removal of SMX at 27 °C; (d) summary of degradation of SMX under visible light by Bi-MOF, Ag^+/Bi-MOF, NH_4^+/Ag^+/Bi-MOF.

with other molecules within the MOF. Because the Bi^{3+} ions in bismuth-MOF are "locked" within the MOF structure, they are not readily available to directly form complexes with other molecules like SMX. This limits SMX's ability to interact directly with Bi^{3+} within the MOF to form a complex (Fig. 5a).

In contrast, when Ag^+ is present, it exists as a free ion in solution and can directly interact with SMX. Ag^+ has a high affinity for functional groups in SMX (such as the sulfonamide $-SO_2NH_2$ and amino $-NH_2$ groups). This is reflected in the peak shift from 263 nm and 201 nm to 240 nm and 203 nm (Fig. 5b). SMX can easily form a complex with Ag^+ due to Ag^+'s flexible nature and its ability to readily interact with the functional groups in the SMX molecule. This complex can form in solution and is not constrained by a fixed structure like Bi-MOF.

3.2.3 Effect of pH and NH_4^+ competition. When NH_4^+ is added to the system, it can inhibit sulfamethoxazole from forming a complex with Ag^+. NH_4^+ is typically present in the solution as NH_4Cl or NH_4OH, which can influence the pH of the environment. When NH_4^+ is added, the pH of the solution may decrease, becoming more acidic. In an acidic environment, functional groups like $-SO_2NH_2$ and $-NH_2$ in SMX can become protonated. At lower pH, the $-NH_2$ group in SMX can gain a proton, becoming $-NH_3^+$. This reduces the ability of this group to bind with Ag^+ because the $-NH_3^+$ group is less capable of interacting with Ag^+ compared to the neutral $-NH_2$ group (Fig. 5c).

NH_4^+ can interact with Ag^+ ions in the solution, reducing the availability of Ag^+ to interact with SMX. Although NH_4^+ does not strongly bind with Ag^+, it can alter the distribution of Ag^+ in the solution. In the presence of NH_4^+, Ag^+ may form weak interactions or be surrounded by water molecules and other anions, reducing its likelihood of directly interacting with SMX, thereby diminishing the potential for complex formation.[42,43]

In a solution containing NH_4^+, competitive reactions may occur. NH_4^+ may compete with SMX for binding sites on Ag^+ or create weak interactions with Ag^+, making Ag^+ less likely to form a complex with SMX. Additionally, NH_4^+ can create a more complex environment by increasing the presence of other ions, altering the chemical equilibrium in the solution, and decreasing the potential for complex formation between SMX and Ag^+.

3.3. Photocatalytic efficiency of Bi-MOF derivatives and reusability

3.3.1 Reusability. Fig. 6a illustrates the reusability of the NH_4^+/Ag^+/Bi-MOF material in degrading the antibiotic tetracycline. Reusability reflects the material's ability to maintain its antibiotic degradation efficiency over multiple cycles of use. In the first cycle, 98.6% of TC was degraded, and this value remained stable at 97.6% (cycle 2), 96.5% (cycle 3), and 96.1% (cycle 4). The NH_4^+/Ag^+/Bi-MOF material has demonstrated the ability to maintain high photocatalytic activity through multiple

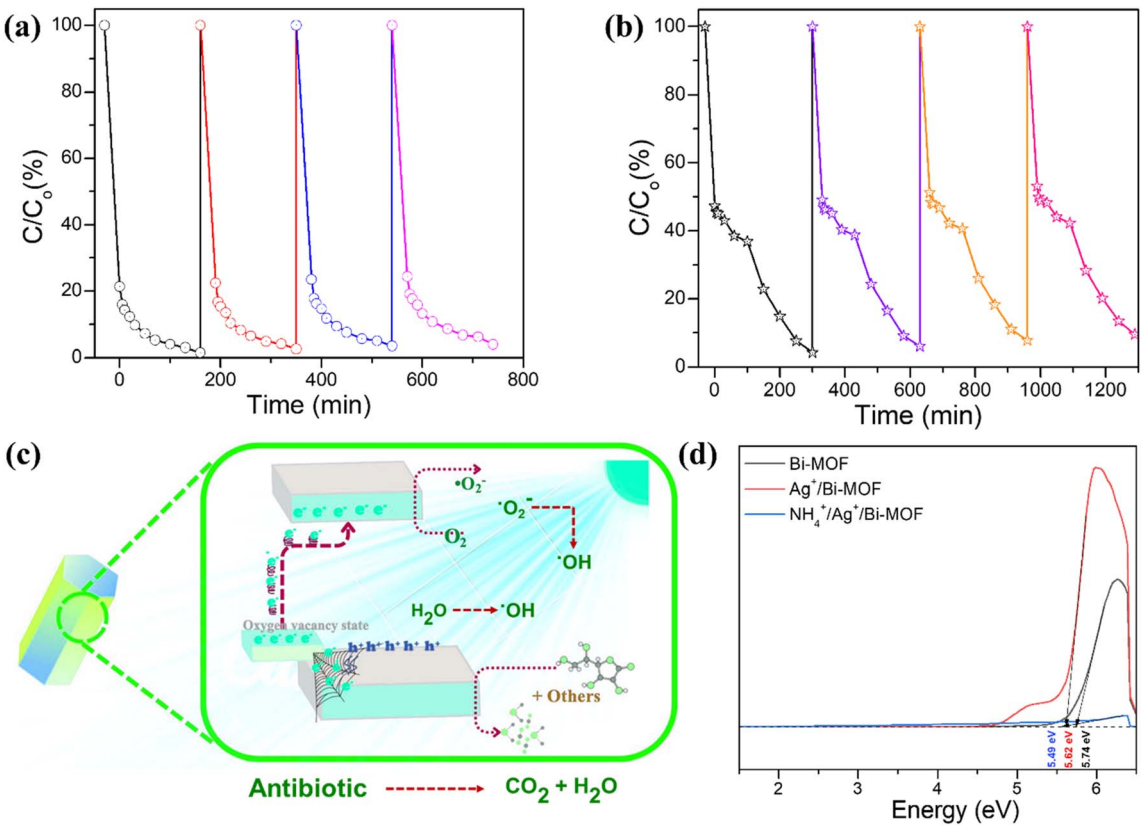

Fig. 6 (a) Reusability of NH_4^+/Ag^+/Bi-MOF for the antibiotic tetracycline; (b) reusability of Ag^+/Bi-MOF for the antibiotic sulfamethoxazole; (c) proposed mechanism for antibiotic degradation by Bi-MOF derivatives; (d) bandgap of Bi-MOF, Ag^+/Bi-MOF, NH_4^+/Ag^+/Bi-MOF.

reuse cycles, indicating its stability and practical potential for environmental treatment applications.

The reusability of the Ag^+/Bi-MOF material in degrading the antibiotic sulfamethoxazole is illustrated in Fig. 6b. The Ag^+/Bi-MOF material also demonstrates strong reusability for difficult-to-degrade antibiotics like SMX, with its degradation efficiency showing minimal reduction after multiple cycles. Specifically, the first cycle achieved a degradation rate of 95.3%, and the efficiency slightly decreased in the subsequent cycles, with 93.9%, 92.2%, and 90.5% after the next three cycles, respectively. This indicates that Ag^+/Bi-MOF is a durable photocatalyst, suitable for long-term application in treating hard-to-degrade antibiotics like SMX.

When the Bi-MOF derivatives (such as Ag^+/Bi-MOF or NH_4^+/Ag^+/Bi-MOF) are exposed to visible light, they absorb light energy and generate electron–hole pairs within their structure. Ag^+ (silver ion) plays a crucial role in preventing the recombination of electron–hole pairs by creating electron traps.[44] This allows the free electrons and holes to exist longer, enhancing photocatalytic activity. The excited electrons from the conduction band can participate in reduction reactions, while the holes in the valence band can engage in oxidation reactions. These reactions produce free radicals such as ·OH (hydroxyl radicals) or $O_2^{\cdot-}$ (superoxide radicals), which can degrade antibiotic molecules like TC or SMX. These free radicals attack the antibiotic molecules, breaking the chemical bonds in their molecular structure, leading to the degradation of the antibiotics.[45,46] After the catalytic process is complete, the catalyst can be reused in subsequent cycles without significant loss in efficiency (Fig. 6c).

Fig. 6d shows that modifying the chemical structure of Bi-MOF by adding Ag^+ and NH_4^+ can alter the material's bandgap, which in turn affects its light absorption and photocatalytic efficiency. A smaller bandgap allows the material to absorb light more effectively and generate more free radicals, enhancing its ability to degrade organic pollutants. This change indicates the potential of adjusting the Bi-MOF structure to improve catalytic performance, especially in environmental treatment and the degradation of persistent pollutants like antibiotics.[47,48] The bandgap of Bi-MOF reflects its ability to absorb visible light, but its efficiency is not high due to the rapid recombination of electron–hole pairs. This leads to the generation of fewer free radicals and, consequently, a lower antibiotic degradation efficiency compared to other derivatives.[49,50] When Ag^+ is added to the Bi-MOF structure, the material's bandgap may change, typically becoming narrower. This narrowing of the bandgap allows Ag^+/Bi-MOF to absorb light at longer wavelengths, meaning it can absorb light more effectively in the visible range. Ag^+ also helps create electron traps, preventing the rapid recombination of electron–hole pairs, and thereby enhancing photocatalytic efficiency. As a result, Ag^+/Bi-MOF can more effectively degrade organic pollutants such as antibiotics. When NH_4^+ is added along with Ag^+, the bandgap may continue to change, usually with a slight adjustment in energy and catalytic efficiency. NH_4^+ can affect the surface chemistry of the material, influencing the absorption and degradation processes of pollutants. The combination of Ag^+ and NH_4^+ can lead to adjustments in the bandgap and surface properties of the material, making NH_4^+/Ag^+/Bi-MOF a more effective photocatalyst compared to the original Bi-MOF.

Based on the changes in the UV-Vis spectra and previous studies on the photocatalytic degradation mechanism of TC, the potential intermediate products may include deamination and *N*-demethylation products, ring-opening products, and carboxylic acid products.[51–53] In addition, the UV-Vis spectra reveal the appearance and disappearance of intermediate products during the photocatalytic degradation of SMX, with potential intermediates including ring cleavage products, desulfonation products, hydroxylation, and oxidation products (Table 1).[54–56]

3.3.2 Photocatalytic efficiency. The COD and TOC experiments were conducted to evaluate the mineralization of TC and SMX by the NH_4^+/Ag^+/Bi-MOF photocatalyst. As shown in Fig. 7, the COD reductions for TC and SMX were 89.5% and 86.4%,

Table 1 A compilation of intermediate degradation products of tetracycline and sulfamethoxazole during the photocatalytic process using modified MOF materials

No	Antibiotic	Intermediate compounds	Nanomaterial	Ref.
01	Tetracycline	Epimers and hydroxylated tetracyclines	MOF-801/GO composite	57
02	Tetracycline	Dehydroxylation, 6 deamidation, ring opening, oxidation and *N*-demethylation reactions	MIL-88B on NH_2-MIL-125	58
03	Tetracycline	Ring-opened tetracycline intermediates	$ZnIn_2S_4$/MOF-525 (zirconium-based porphyrin metal organic frameworks)	51
04	Tetracycline	Anhydrotetracycline, hydroxytetracycline, 3-amino-5-methylphenol, benzoic acid derivative	3D Cu-MOFs	52
05	Tetracycline	Deamination and *N*-demethylation products, ring-opening products, carboxylic acids	NH2-MIL-88B(Fe)@MIL-100(Fe)	53
06	Sulfamethoxazole	*N*-Hydroxysulfamethoxazole, sulfamethoxazole sulfinic acid derivative, 4-nitrophenol sulfonamide derivative, 3-amino-5-methylisoxazole	Diatomite-supported hydroxyl-modified UIO-66	59
07	Sulfamethoxazole	Ring cleavage products, desulfonation products, hydroxylation and oxidation products	MIL-101(Fe) supported Mo single-atom	54
08	Sulfamethoxazole	Hydroxy-*N*-sulfamoyl-benzene derivative, 4-nitrobenzoic acid derivative, hydroxylated sulfamethoxazole, 3-amino-5-methylisoxazole	*N*-Doped ZnO carbon skeleton@Bi_2MoO_6 S-scheme heterojunction	55
09	Sulfamethoxazole	Hydroxylated SMX, benzenesulfonamide derivatives, and 3-amino-5-methylisoxazole	MOF derivate Fe@Cs	56

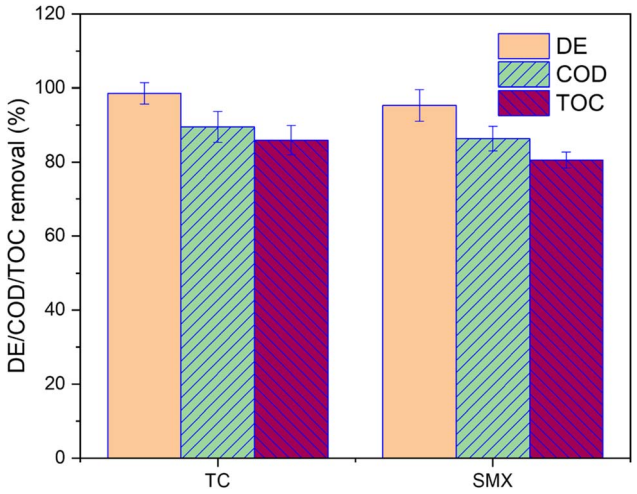

Fig. 7 Photocatalytic efficiency and mineralization performance of NH_4^+/Ag^+/Bi-MOF for TC and SMX under visible light irradiation for 160 min.

respectively, indicating substantial oxidation of the organic pollutants and their intermediates. The TOC reductions were 85.97% for TC and 80.56% for SMX, reflecting effective mineralization. The removal of COD and TOC was lower than the degradation efficiency (DE), which was 98.6% for TC and 95.3% for SMX, due to the formation of sequential organic intermediates during the process before the complete breakdown of TC and SMX into carbon dioxide and other simpler products.[60] These results demonstrate the capability of NH_4^+/Ag^+/Bi-MOF to effectively degrade and mineralize TC and SMX, with the photocatalytic process leading to the conversion of the pollutants into simpler, less harmful by-products.

The photocatalytic efficiency of Bi-MOFs is primarily associated with their large surface area, tunable porosity, and unique electronic properties that facilitate visible light absorption and promote effective charge separation. These characteristics allow Bi-MOFs to function as efficient photocatalysts in the degradation of organic pollutants, including antibiotics such as tetracycline and sulfamethoxazole. The introduction of silver ions (Ag^+) into the Bi-MOF framework has significantly enhanced the photocatalytic efficiency of the material. Ag^+ ions are known for their ability to improve charge separation by acting as electron traps, thereby reducing the recombination rate of electron–hole pairs generated during photocatalysis. This leads to a more efficient degradation process of organic pollutants under visible light. Specifically, the Ag^+/Bi-MOF derivative exhibited superior photocatalytic efficiency in the degradation of TC and SMX compared to the unmodified Bi-MOF.

Additionally, the incorporation of ammonium ions (NH_4^+) along with Ag^+ into the Bi-MOF structure (forming NH_4^+/Ag^+/Bi-MOF) introduced further modifications to the surface chemistry of the catalyst. NH_4^+ ions can alter the pH of the surrounding environment and influence the interaction between the catalyst and the target pollutants. This impacts the adsorption and degradation processes, resulting in significant photocatalytic activity observed in NH_4^+/Ag^+/Bi-MOF. Experimental results showed that both Ag^+/Bi-MOF and NH_4^+/Ag^+/Bi-MOF derivatives exhibited higher photocatalytic efficiency than the original Bi-MOF, with Ag^+/Bi-MOF showing the most promising performance. These findings highlight the potential of modifying the Bi-MOF structure with specific metal ions to enhance their photocatalytic capabilities.

3.3.2.1 Kinetic model. The kinetic model for the photocatalytic activity of Bi-MOF, Ag^+/Bi-MOF, and NH_4^+/Ag^+/Bi-MOF in degrading of tetracycline fitted by a power law equation based on the Korsmeyer–Peppas (K–P) model, which was usually used to predict the non-Fickian model:

$$\frac{Q_t}{Q_\infty} = kt^n \quad (4)$$

where Q_t/Q_∞ is a fraction of TC degradation at time t, k is the relaxation rate constant, and n is the release exponent.[61,62] According to Fig. 8a, the K–P model demonstrated a good fit for the photocatalytic activity of (i) Bi-MOF, $k = 76.9$, (ii) Ag^+/Bi-MOF, $k = 24.4$, and (iii) NH_4^+/Ag^+/Bi-MOF, $k = 14.1$.

The kinetic model for the photocatalytic activity of SMX in Fig. 8b follows the equation:

$$\frac{Q_t}{Q_\infty} = at + b \quad (5)$$

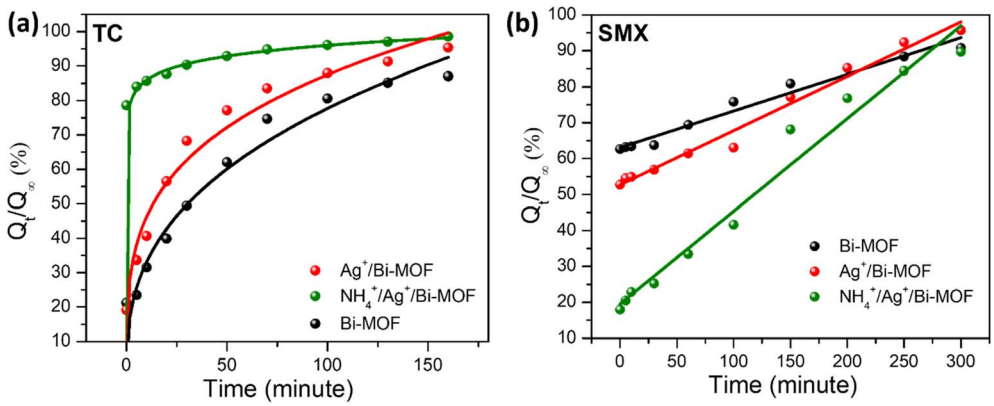

Fig. 8 Figure illustrates the kinetic model for the photocatalytic activity of Bi-MOF, Ag^+/Bi-MOF, and NH_4^+/Ag^+/Bi-MOF in degrading (a) tetracycline (TC) and (b) sulfamethoxazole (SMX) under irradiation. The curves represent the fitting of experimental data to kinetic equations.

where Q_t/Q_∞ is the percentage of SMX degradation relative to the total amount that can be degraded at time t, and a is the slope, representing the degradation rate of the pollutant.

Bi-MOF (black) has the smallest slope, indicating the slowest reaction rate. Meanwhile, Ag^+/Bi-MOF (red) shows a steeper slope, demonstrating an improved reaction rate due to the presence of Ag^+. Notably, NH_4^+/Ag^+/Bi-MOF (green) exhibits the steepest slope, confirming that the combination of NH_4^+ and Ag^+ significantly enhances the photocatalytic efficiency.

4. Conclusions

In this study, we successfully synthesized and characterized bismuth-based metal–organic frameworks and their derivatives, specifically Ag^+/Bi-MOF and NH_4^+/Ag^+/Bi-MOF, using a solvothermal method. The photocatalytic efficiency of these materials was evaluated in the degradation of tetracycline and sulfamethoxazole under visible light. The results showed that Bi-MOFs have significant potential as photocatalysts due to their large surface area, tunable porosity, and favorable electronic properties for visible light absorption. Among the synthesized materials, Ag^+/Bi-MOF demonstrated superior photocatalytic efficiency, attributed to enhanced charge separation and improved light absorption due to the incorporation of silver ions. NH_4^+/Ag^+/Bi-MOF also exhibited significant photocatalytic activity, with ammonium ions affecting the surface chemistry of the catalyst and influencing the adsorption and degradation processes. These findings underscore the importance of modifying the MOF structure with metal ions like Ag^+ to enhance photocatalytic performance. Reusability tests also confirmed the practical potential of these photocatalysts, as they maintained high degradation efficiency over multiple cycles. This highlights their applicability in real-world environmental treatment technologies, particularly in the removal of persistent organic pollutants such as TC and SMX.

Data availability

The data that support the findings of this study are available on request from the corresponding author. The data are not publicly available due to restrictions *e.g.*, their containing information that could compromise the privacy of research participants.

Conflicts of interest

There are no conflicts to declare.

Acknowledgements

The authors acknowledge support from Nguyen Tat Thanh University in Ho Chi Minh City, Vietnam.

References

1 A. Mukhopadhyay, S. Duttagupta and A. Mukherjee, *J. Environ. Chem. Eng.*, 2022, **10**, 107560.
2 A. Hussain, S. Ashique, M. Zaheen Hassan, O. Afzal, Y. I. Asiri, P. Kumar, K. Dua, T. J. Webster, A. S. A. Altamimi and M. A. Altamimi, *J. Mol. Liq.*, 2023, **389**, 122905.
3 B. Wang, Z. Xu and B. Dong, *J. Hazard. Mater.*, 2024, **469**, 133925.
4 A. E. Gahrouei, S. Vakili, A. Zandifar and S. Pourebrahimi, *Environ. Res.*, 2024, **252**, 119029.
5 A. Redwan Haque, M. Sarker, R. Das, M. A. K. Azad and M. M. Hasan, *Int. J. Environ. Anal. Chem.*, 2023, **103**, 3704–3721.
6 S. Zhang, H. Zheng and P. G. Tratnyek, *Nat. Water*, 2023, **1**, 666–681.
7 C. Yu, Z. Xiong, H. Zhou, P. Zhou, H. Zhang, R. Huang, G. Yao and B. Lai, *Chem. Eng. J.*, 2022, **433**, 133802.
8 A. Intisar, A. Ramzan, S. Hafeez, N. Hussain, M. Irfan, N. Shakeel, K. A. Gill, A. Iqbal, M. Janczarek and T. Jesionowski, *Chemosphere*, 2023, **336**, 139203.
9 M. A. Al-Nuaim, A. A. Alwasiti and Z. Y. Shnain, *Chem. Pap.*, 2023, **77**, 677–701.
10 V. A. Tran, G. N. L. Vo, V. D. Doan, N. C. Thanh, T. D. Lam and V. T. Le, *Microchem. J.*, 2024, **197**, 109852.
11 V. A. Tran, V. Thuan Le, V. D. Doan and G. N. L. Vo, *Pharmaceutics*, 2023, **15**, 931.
12 F. Yang, M. Du, K. Yin, Z. Qiu, J. Zhao, C. Liu, G. Zhang, Y. Gao and H. Pang, *Small*, 2022, **18**, 2105715.
13 N. A. Nordin, M. A. Mohamed, M. N. I. Salehmin and S. F. Mohd Yusoff, *Coord. Chem. Rev.*, 2022, **468**, 214639.
14 P. M. Stanley, J. Haimerl, N. B. Shustova, R. A. Fischer and J. Warnan, *Nat. Chem.*, 2022, **14**, 1342–1356.
15 J. Zou, Y. Shao, X. Hu, H. Zhang, S. Ye and J. Li, *Chem. Eng. J.*, 2024, **484**, 149337.
16 V. Anh Tran, T. Khoa Phung, V. Thuan Le, T. Ky Vo, T. Tai Nguyen, T. Anh Nga Nguyen, D. Quoc Viet, V. Quang Hieu and T.-T. Thi Vo, *Mater. Lett.*, 2021, **284**, 128902.
17 V. Anh Tran, L. T. Nhu Quynh, T.-T. Thi Vo, P. A. Nguyen, T. N. Don, Y. Vasseghian, H. Phan and S.-W. Lee, *Environ. Res.*, 2022, **204**, 112364.
18 V. A. Tran and S.-W. Lee, *RSC Adv.*, 2021, **11**, 9222–9234.
19 M. Liu, P. Ye, M. Wang, L. Wang, C. Wu, J. Xu and Y. Chen, *J. Environ. Chem. Eng.*, 2022, **10**, 108436.
20 D. Pattappan, C.-J. Liao, R. S. Kumar, S. Ramesh, R. T. R. Kumar, W. Yang, Y. Haldorai and Y.-T. Lai, *J. Taiwan Inst. Chem. Eng.*, 2024, **165**, 105725.
21 S. K. Gopinathan, P. Vishwa, G. D. Nessim, I. Udachyan and S. Kandaiah, *ACS Appl. Energy Mater.*, 2024, **7**, 6807–6820.
22 M. Kocsis, M. Szabados, S. B. Ötvös, G. F. Samu, Z. Fogarassy, B. Pécz, Á. Kukovecz, Z. Kónya, P. Sipos, I. Pálinkó and G. Varga, *J. Catal.*, 2022, **414**, 163–178.
23 V. Thakur, S. Singh, P. Kumar, S. Rawat, V. Chandra Srivastava, S.-L. Lo and U. Lavrenčič Štangar, *Chem. Eng. J.*, 2023, **475**, 146100.
24 R. K. Chava, Y. Im and M. Kang, *J. Mater. Chem. A*, 2024, **12**, 18498–18511.
25 N. K. Sompalli, Y. Li, J. Li and S. Kuppusamy, *Environ. Res.*, 2024, **259**, 119532.

26 M. B. Chabalala, B. M. Mothudi and B. Ntsendwana, *J. Photochem. Photobiol., A*, 2024, **447**, 115244.
27 V. A. Tran, A. N. Kadam and S.-W. Lee, *J. Alloys Compd.*, 2020, **835**, 155414.
28 S. Dong, L. Wang, W. Lou, Y. Shi, Z. Cao, Y. Zhang and J. Sun, *Ultrason. Sonochem.*, 2022, **91**, 106223.
29 L. Ding, Y. Li, Y. Ding, F. Bai, B. Jia, H. Li and X. Wang, *Appl. Surf. Sci.*, 2023, **624**, 157100.
30 M.-C. Guo, W.-D. Zhong, T. Wu, W.-D. Han, X.-S. Gao and X.-M. Ren, *J. Solid State Chem.*, 2022, **309**, 123005.
31 R. Huang, Z. Zhou, X. Lan, F. K. Tang, T. Cheng, H. Sun, K. Cham-Fai Leung, X. Li and L. Jin, *Mater. Today Bio*, 2023, **18**, 100507.
32 W. A. Mohamed, J. Chakraborty, L. Bourda, R. Lavendomme, C. Liu, R. Morent, N. De Geyter, K. Van Hecke, A. M. Kaczmarek and P. Van Der Voort, *J. Am. Chem. Soc.*, 2024, **146**, 13113–13125.
33 J. Jiang, W. Wei, Y. Tang, S. Yang, X. Wang, Y. Xu and L. Ai, *Inorg. Chem.*, 2022, **61**, 19847–19856.
34 L. Liu, K. Yao, J. Fu, Y. Huang, N. Li and H. Liang, *Colloids Surf., A*, 2022, **633**, 127840.
35 J. Jiang, Y. Xu, C. Tang, X. Wang, W. Wei and L. Ai, *Desalination*, 2023, **560**, 116680.
36 W. Liu, J. Guan, B. Kong, H. Lu, Y. Wu, X. Qin, H. Jiang and X. Liu, *J. Solid State Electrochem.*, 2023, **27**, 3393–3404.
37 Z. Gao, M. Hou, Y. Shi, L. Li, Q. Sun, S. Yang, Z. Jiang, W. Yang, Z. Zhang and W. Hu, *Chem. Sci.*, 2023, **14**, 6860–6866.
38 H. Liu, Z. Huang, W. Zhang, C. Zhang, S. Wang and W. Wang, *Chemosphere*, 2024, **359**, 142274.
39 Y. Li, D. Han, Z. Wang and F. Gu, *ACS Appl. Mater. Interfaces*, 2024, **16**, 7080–7096.
40 M. Chen, S. Wei, J. Wu, J. Li, B. Fu and X. Zhu, *Colloids Surf., A*, 2023, **664**, 131186.
41 Z. Tan, C. Shi, Z. Shi, H. Yang, J. yang, C. Wu and D. Wang, *J. Alloys Compd.*, 2024, **1005**, 176049.
42 T.-H. Ngo, P.-N.-M. Le, C.-H. Truong, N.-D.-T. Huynh, T.-H. Tran, V.-H. Luan, B.-T. Dang, M. Rafie Johan, S. Sagadevan and M.-V. Le, *J. Photochem. Photobiol., A*, 2024, **446**, 115157.
43 M. Wang, G. Lu, R. Jiang, T. Dang and J. Liu, *J. Colloid Interface Sci.*, 2022, **622**, 995–1007.
44 X. Zhang, S. Jiang, L. X. Sun, Y. H. Xing and F. Y. Bai, *J. Mol. Struct.*, 2022, **1270**, 133895.
45 X. Yue, L. Cheng, F. Li, J. Fan and Q. Xiang, *Angew. Chem., Int. Ed.*, 2022, **61**, e202208414.
46 B. Zhang, H. Xu, M. Wang, L. Su, S. Zhang, Y. Zhang and Q. Wang, *J. Environ. Chem. Eng.*, 2022, **10**, 108469.
47 B. Zhang, H. Xu, M. Wang, L. Su, C. Wu and Q. Wang, *J. Environ. Chem. Eng.*, 2023, **11**, 110417.
48 W. Lou, L. Wang, S. Dong, Z. cao, J. Sun and Y. Zhang, *Opt. Mater.*, 2022, **126**, 112168.
49 L. Ding, Y. Ding, F. Bai, G. Chen, S. Zhang, X. Yang, H. Li and X. Wang, *Inorg. Chem.*, 2023, **62**, 2289–2303.
50 G. Huang, Z. Li, K. Liu, Y. Zhang, X. Tang, Q. Peng, J. Huang and G. Zhang, *J. Water Process. Eng.*, 2022, **46**, 102636.
51 X. Zhang, Z. Liu, B. Shao, T. Wu, Y. Pan, S. Luo, M. He, L. Ge, J. Sun, C. Cheng and J. Huang, *Environ. Sci. Pollut. Res. Int.*, 2023, **30**, 67647–67661.
52 R. Zhou, C. Zou, Y. Wang, Z. Zhou, M. Liu and Y. Ji, *Water, Air, Soil Pollut.*, 2024, **235**, 295.
53 Q. Zhang, J. Xu, X. Ma, J. Xu, Z. Yun, Q. Zuo and L. Wang, *J. Water Process. Eng.*, 2021, **44**, 102364.
54 W. Kong, Z. Liu, J. Wu, C. Wen, J. Yan, Y. Gao, G. Li, X. Wang and M. Huo, *Process Saf. Environ. Prot.*, 2025, 106778, DOI: **10.1016/j.psep.2025.106778**.
55 A. Wang, J. Ni, W. Wang, X. Wang, D. Liu and Q. Zhu, *J. Hazard. Mater.*, 2022, **426**, 128106.
56 M. Pu, J. Wan, F. Zhang, M. L. Brusseau, D. Ye and J. Niu, *J. Hazard. Mater.*, 2021, **414**, 125598.
57 Z. Wu, Z. Chen, J. Chen, X. Ning, P. Chen, H. Jiang and H. Qiu, *Environ. Sci.: Nano*, 2022, **9**, 4609–4618.
58 T. Gao, H. Zhang, X. Zhao, S. Xiao, Z. Zhang and S. Yu, *Appl. Surf. Sci.*, 2024, **651**, 159227.
59 H.-L. Liu, Y. Zhang, X.-X. Lv, M.-S. Cui, K.-P. Cui, Z.-L. Dai, B. Wang, R. Weerasooriya and X. Chen, *Nanomaterials*, 2023, **13**(24), 3116.
60 S. Singla, P. Singh, S. Basu and P. Devi, *Mater. Chem. Phys.*, 2023, **295**, 127111.
61 I. Izquierdo-Barba, E. Sousa, J. C. Doadrio, A. L. Doadrio, J. P. Pariente, A. Martínez, F. Babonneau and M. Vallet-Regí, *J. Sol-Gel Sci. Technol.*, 2009, **50**, 421–429.
62 P. Costa and J. M. Sousa Lobo, *Eur. J. Pharm. Sci.*, 2001, **13**, 123–133.